Physica B 475 (2015) 140–147

Contents lists available at ScienceDirect

Physica B

journal homepage: www.elsevier.com/locate/physb

Short-range order in *ab initio* computer generated amorphous and liquid Cu–Zr alloys: A new approach

Jonathan Galván-Colín [a], Ariel A. Valladares [a,*], Renela M. Valladares [b], Alexander Valladares [b]

[a] Instituto de Investigaciones en Materiales, Universidad Nacional Autónoma de México, Apartado Postal 70-360, México, D.F. 04510, México
[b] Facultad de Ciencias, Universidad Nacional Autónoma de México, Apartado Postal 70-542, México, D.F. 04510, México

ARTICLE INFO

Article history:
Received 10 March 2015
Received in revised form
8 July 2015
Accepted 26 July 2015
Available online 29 July 2015

Keywords:
Ab initio molecular dynamics
Amorphous alloys
Bulk metallic glass
Pair distribution function

ABSTRACT

Using *ab initio* molecular dynamics and a new approach based on the *undermelt-quench* method we generated amorphous and liquid samples of Cu_xZr_{100-x} (x=64, 50, 36) alloys. We characterized the topology of our resulting structures by means of the pair distribution function and the bond-angle distribution; a coordination number distribution was also calculated. Our results for both amorphous and liquids agree well with experiment. Dependence of short-range order with the concentration is reported. We found that icosahedron-like geometry plays a major role whenever the alloys are Cu-rich or Zr-rich disregarding if the samples are amorphous or liquid. The validation of these results, in turn would let us calculate other properties so far disregarded in the literature.

1. Introduction

Much attention has been paid to amorphous metallic systems in recent years. However, these systems have been studied since 1960 when Duwez et al. were the first to report the experimental generation of the $Au_{75}Si_{25}$ metallic glass [1].

In the late 1980s a large variety of multicomponent amorphous alloys were available: binary, ternary, etc. [2]. In spite of this, the simplicity of binary alloys has been an appealing factor to study them due to the limited number of constituents; particularly, the Cu–Zr alloys have become very prominent since they are good formers of glassy samples [3–7]. Among the experimental works concerning the characterization of the Cu–Zr alloys—particularly the $Cu_{64}Zr_{36}$ concentration—the work by Wang et al. [8] is to be noted. They prepared both 1 mm rods and ribbons with a concentration of $Cu_{64.5}Zr_{35.5}$ and analyzed it *via* X-ray diffraction (XRD). They found that the major number of polyhedra arrangements present in their samples were icosahedron-like dense packing clusters with a concentration of $Cu_{7.75}Zr_{5.25}$ and with minor distortions.

In another experimental work performed by Mattern et al. [7] both XRD and neutron dispersion (ND) of an ingot of $Cu_{65}Zr_{35}$ were reported, finding a total coordination number of 13.2. Unlike Wang et al., they found a large variety of polyhedra arrangements in their local structures, thus arguing that there was no obvious indication suggesting the existence of a dominant cluster structure. In addition there are other experimental studies where coordination numbers and first neighbor distances were reported using XRD [9,10]; however no information about the local geometry was provided.

Amorphous Cu–Zr system has not only been studied experimentally, but also from the simulational point of view by means of dense random packing [9], reverse Monte Carlo (RMC) [7,8], first principles molecular dynamics [8,11] and other approaches which involve tight-binding, second moment approximation or classical molecular dynamics [12–18]. First principles methods usually involve melting the sample with a subsequent fast quenching stage to avoid crystallization.

On the other hand, it is interesting to study the liquid phase since there is a debate about short-range order (SRO) in the melt [19]; specifically icosahedron-like ordering has been related to glass forming ability upon cooling since such packing becomes highly stable in the glass, reducing atomic mobility and enhancing the vitrification of the material. In addition, there was a recent study of liquid Cu_xZr_{100-x} (x=80, 72, 65, 57, 50, 33.3) by *ab initio* molecular dynamics reported by Hao et al. [20]. They performed correlated low diffusivities in the liquid with the presence of some specific clusters including icosahedra which, they argued, were responsible for slowing the dynamics in the composition range $50 \leq x \leq 70$. Therefore, by simulating the liquid we can verify

* Corresponding author. Fax: +52 5556224636.
E-mail addresses: jgcolin@ciencias.unam.mx (J. Galván-Colín), valladar@unam.mx (A.A. Valladares).

http://dx.doi.org/10.1016/j.physb.2015.07.027
0921-4526/

whether icosahedron-like ordering prevails upon phase changing and concentration variations since such SRO geometry has been considered as preponderant.

In the present work we have applied two variants of an *ab initio* process which has demonstrated to lead to good results for semiconducting amorphous structures [21–27] and metallic structures such as amorphous and liquid aluminum [28,29], the *undermelt-quench approach*, to generate amorphous and liquid Cu_xZr_{100-x} (x=64, 50, 36) alloys. We report the corresponding total and partial pair distribution functions (PDF & pPDFs) in order to study the atomic environment in each phase. Inasmuch as the presence of icosahedral clustering in the Cu–Zr metallic glass has been discussed [7,8,30], we performed a bond-angle distribution (BAD) analysis to compare the icosahedron-like ordering present in both liquid and amorphous phases since this method has been useful in the analysis of the topology of metallic glasses [31–33]. With this we could track the evolution of icosahedron-like SRO as a function of the phase of the system and the concentration of each constituent. We ponder over agreements and discrepancies with experimental data and with other theoretical results.

Our new approach generates reliable amorphous and liquid transition metal alloys that allows us the calculation of other properties, such as the electronic and vibrational ones [34] which have been almost thoroughly disregarded in the literature and which might lead to other potential applications of these materials besides their well-known mechanical ones.

2. Methodology

In order to computationally generate the liquid and amorphous samples we used DMol^3 [35–37], a DFT-based code included in the Materials Studio Suite. We used the local density approximation (LDA) and the exchange-correlation functional due to Perdew and Wang [38]. Spin-unrestricted calculations with a double-numerical basis set that include *d* polarization functions (dnd) were employed [35]. In order to optimize the computational resources—inherent to first principles calculations—we used *dspp* (DFT semi-local pseudopotentials) which replaces the effects of core electrons by a simple potential adding a certain degree of relativistic effects [36]. Pseudopotentials allow us to reduce CPU time without compromising the quality of the calculations. Cut-off distances were set at 4.4 Å for Cu and 5.3 Å for Zr and an NVT Nosé–Hoover thermostat along with the Verlet velocity integrator algorithm was used. Periodic boundary conditions were also incorporated.

For all our simulations we use two different time steps: the default time step (DTS), which is proportional to $\sqrt{m_{min}/5}$ where m_{min} is the smallest mass in the system (Cu), DTS was then 3.57 fs; and three times the DTS: 10.71 fs (3DTS) in order to improve the dynamical process during melting and heating. We did this in order to verify how the time step affected the resulting structures generated by the variants of the *undermelt-quench* process, since it is often argued that large time steps result in error calculations or in colliding atoms that would destabilize the structure.

The *undermelt-quench* method, as reported by Valladares et al. involves a linear heating of the simulation cell to a few Kelvin below the melting point or the corresponding *liquidus*, and well above the glass transition temperature in 100 steps. After that, the sample is immediately cooled down linearly to 0 K with a cooling rate equal to the heating rate. During this process, the atoms are allowed to move within the simulation cell at constant volume and at atmospheric pressure. Once this heating/cooling stage is completed the samples are subjected to annealing cycles at 300 K with intermediate quenching stages using the same cooling rate as in the first cooling period [21]. The variants applied to our simulation cells are described below.

Moreover, we know that the *undermelt-quench* method works best with time steps larger than the default ones in the case of semiconductors, therefore we are exploring its transferability to transition metal systems as well.

We started from cubic supercells with 108 atoms of Cu, from which either 39, 54 or 69 atoms were randomly substituted by atoms of Zr in order to have the corresponding concentrations: $Cu_{64}Zr_{36}$ (64–36), $Cu_{50}Zr_{50}$ (50–50) and $Cu_{36}Zr_{64}$ (36–64), whose corresponding densities were taken from experiment [7]: 7.75 g/cm^3, 7.33 g/cm^3 and 7.01 g/cm^3. The same initial 108-atom supercells were used both to generate the liquid and the amorphous samples, contrary to some studies where either the crystalline or a linearly adjusted density is used.

2.1. Amorphous samples

To generate the amorphous samples with DTS the initial supercells were linearly heated in 300 steps from 300 K up to 1223 K ($Cu_{64}Zr_{36}$), 1198 K ($Cu_{50}Zr_{50}$) and 1263 K ($Cu_{36}Zr_{64}$); these temperatures are a few Kelvin below the corresponding *liquidus* of the experimental value reported in the phase diagrams of the alloys [39] (*undermelt* stage), forcing the structures to quickly randomize as the temperature rises. Then the samples were cooled down to a few Kelvin in 397 ($Cu_{64}Zr_{36}$), 399 ($Cu_{50}Zr_{50}$) and 393 steps ($Cu_{36}Zr_{64}$) (*quench* stage). This number of corresponding cooling steps for each alloy was set in order to have the same cooling rate as in the heating stage. On the other hand, for the samples generated using 3DTS the linear heating was carried out in 100 steps from 300 K to the above mentioned temperatures, but the number of cooling steps were 133 for $Cu_{64}Zr_{36}$ and $Cu_{50}Zr_{50}$ and 131 for $Cu_{36}Zr_{64}$.

Once the *undermelt-quench* process was completed the resulting structures were subjected to a geometry optimization to relax the emerging stresses due to the thermal process and to find the final structures corresponding to the local energy minima. The convergence criterion used was set so that the energy fluctuations were lesser than 1×10^{-5} Ha (1 part in 10^{10}). At this point the atoms were allowed to move in the direction of the forces to minimize the structure energy, but the length of the cell edges was kept constant. No optimization cell was performed since it would lead to a different density value which would not coincide with the experimental value used.

2.2. Liquid samples

For the melting process using DTS the linear heating took 300 steps from 300 K to 1333 K ($Cu_{64}Zr_{36}$), 1308 K ($Cu_{50}Zr_{50}$) and 1373 K ($Cu_{36}Zr_{64}$), while using 3DTS the melting stage was carried out during 100 steps up to the same temperature as with DTS, above their corresponding *liquidus* temperatures of the experimental value reported in the phase diagrams of the alloys [39] in the liquid phase regime. Next, the molten samples were kept at constant temperature during 500 steps (*plateau*), regardless of the time step used. This subsequent constant temperature stage allows the system to become stable in the molten phase as previously reported in liquid aluminum and liquid silicon alloys [28,29].

Contrary to the case of amorphous samples, the geometry optimization was not performed since it would have led to a structure that would not correspond to a representative structure of the liquid. However, since the computer generation leads to several structures that would produce non-distinguishable PDFs, we averaged the last 15 steps of the *plateau* in order to have a better representation of the liquid [29]. This is so because the energy does not change noticeably, therefore, for all practical purposes, these last 15 configurations are energetically equivalent as

previously reported by Díaz-Celaya et al. [29].

For both amorphous and liquid samples generated with DTS and 3DTS we performed two sets of simulations and averaged them afterwards in order to avoid fortuitous results of a single set of simulations. Additionally, to properly compare our resulting amorphous and liquid structures with the experimental results [7,8,19], we weighted our pPDFs using the following expression [40–42]:

$$g(r) = \frac{c_1^2\eta_1^2}{\langle\gamma\rangle^2}g_{11}(r) + \frac{2c_1c_2\eta_1\eta_2}{\langle\gamma\rangle^2}g_{12}(r) + \frac{c_2^2\eta_2^2}{\langle\gamma\rangle^2}g_{22}(r), \quad (1)$$

where c_1 and c_2 are the atomic concentrations of Cu and Zr, respectively; η_1 and η_2 are the Cu and Zr structure factors ($f_i(q=0)$) for X-ray scattering: $f_{Cu} = 29$ and $f_{Zr} = 40$; or the coherence lengths (b_i) for neutron dispersion: $b_{Cu} = 7.718$ and $b_{Zr} = 7.16$ [43]. $g_{ij}(r)$ are the pPDFs with $g_{11} = g_{CuCu}$, $g_{12} = g_{CuZr}$ and $g_{22} = g_{ZrZr}$. Finally, the value of $\langle\gamma\rangle^2$ is

$$\langle f\rangle^2 = \left(\sum_{i=1}^{2} c_i f_i(q)\right)^2 \quad \text{or} \quad \langle b\rangle^2 = \left(\sum_{i=1}^{2} c_i b_i\right)^2 \quad (2)$$

depending on the experimental technique considered.

Furthermore, by taking the first minimum of the corresponding pPDFs as the interatomic distance between each pair of atoms we calculated the BAD for each sample.

We must make clear that our process does not mimic the way an amorphous material is prepared or grown experimentally, but it does have the purpose of generating structures that adequately represent the real ones.

3. Results and discussion

In Fig. 1 we show the pPDFs of the resulting amorphous structures. In the case of the Cu–Cu partial generated with the DTS we see that the peaks up to a distance of 5.5 Å are akin to the crystalline peaks regardless of the concentration. Also for Cu–Cu and Zr–Zr we see that first neighbor distances are shortened with respect to the corresponding crystalline positions (c-Cu and c-Zr) suggesting that in the SRO regime the atoms tend to move to positions which minimize the local energy and *stabilize* the amorphous phase (Table 1). This cannot be analyzed in the case of the $Cu_{64}Zr_{36}$ and $Cu_{36}Zr_{64}$ partial since there is no stable crystal to compare with, except for the B2 crystalline phase of $Cu_{50}Zr_{50}$ (c-50–50); so diffused peaks in the amorphous that barely keep similarity to the B2 crystal are observed.

In the case of the structures generated with 3DTS the peak resemblance with crystalline copper and zirconium is not so evident; we can assert that fluctuations in the PDFs are reduced using 3DTS. Moreover, we notice a displacement to the right in the first peak of Zr–Zr pPDF upon adding zirconium [11] as expected, which is not present in the DTS Zr–Zr pPDF.

As for the total PDFs, in Fig. 2 we notice a clear displacement to larger distances upon adding zirconium which we expected since such element prevails and so does its first neighbor shell distance. In the case of the DTS-generated structures we see a resemblance to crystalline $Cu_{50}Zr_{50}$ peaks which is enhanced in the 50–50 PDF. This behavior is not present in the 3DTS-generated amorphous. Therefore, this suggests that DTS does not fully amorphize our supercells with our *undermelt-quench* method. Furthermore, in the 50–50 concentration this is more evident since, upon quenching, the structure may undergo a phase competition between the amorphous and the stable B2 phase which is present above 930 K according to [39]. Wang et al. previously discussed this stability of $Cu_{50}Zr_{50}$ glass in terms of the competing intermetallic and stable phases [5].

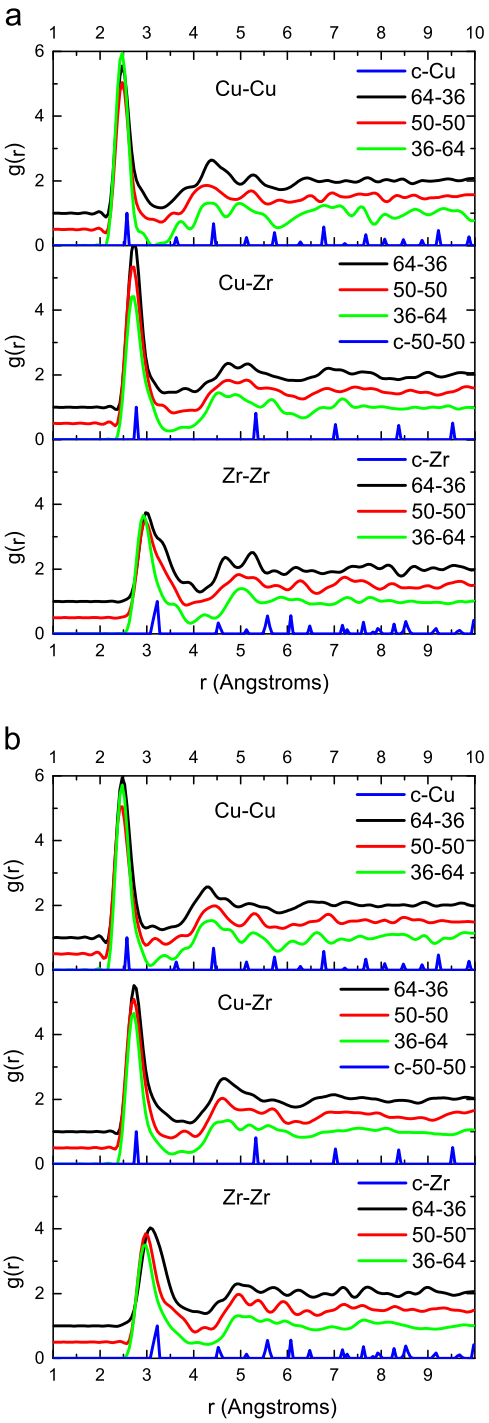

Fig. 1. pPDFs of the resulting amorphous structures using (a) DTS and (b) 3DTS. Cu–Cu and Zr–Zr pPDFs are compared to crystalline Cu and Zr correspondingly. Cu–Zr pPDFs are compared to stable B2 crystalline phase of $Cu_{50}Zr_{50}$.

In our resulting liquid samples we can see from Fig. 3 that the pPDFs exhibit a smoother behavior compared to the amorphous structures, i.e., the first peaks lower in height and are more diffused, meaning that the possible remaining structural memory from the initial ordered configuration vanished. Moreover the bimodal behavior in the second peak almost disappeared. Once more, we observe that the DTS-generated samples, though disordered, have structural remnants of the solid which is reflected in the fluctuations beyond second neighbor distances, which is not the case for the 3DTS-generated liquids.

Table 1
First neighbor distances r_{ij} and coordination numbers N_{ij} for amorphous and liquid DTS- and 3DTS-generated structures.

At.% Cu	64		50		36	
	DTS	3DTS	DTS	3DTS	DTS	3DTS
Amorphous						
r_{CuCu}	2.48	2.48	2.48	2.48	2.48	2.48
r_{CuZr}	2.73	2.73	2.73	2.73	2.73	2.73
r_{ZrZr}	2.98	3.08	2.98	2.98	2.93	2.98
r_{Total}	2.68	2.68	2.68	2.73	2.78	2.78
N_{CuCu}	6.0	6.4	4.1	4.6	3.0	3.6
N_{CuZr}	5.1	5.3	6.6	6.1	7.0	7.7
N_{ZrCu}	8.9	9.4	6.6	6.1	4.0	4.3
N_{ZrZr}	5.8	6.0	7.5	7.5	8.4	8.6
N_{Cu}	11.1	11.7	10.7	10.7	10.0	11.3
N_{Zr}	15.7	15.4	14.1	13.6	12.4	12.9
N_{Total}	12.4	13.0	12.4	12.2	11.5	11.8
Liquid						
r_{CuCu}	2.43	2.43	2.38	2.38	2.43	2.38
r_{CuZr}	2.73	2.73	2.73	2.68	2.68	2.68
r_{ZrZr}	3.13	3.03	2.98	3.13	3.08	2.98
r_{Total}	2.68	2.68	2.78	2.73	2.73	2.83
N_{CuCu}	5.7	6.4	5.0	3.4	3.2	3.1
N_{CuZr}	5.8	5.1	6.0	6.5	7.7	7.3
N_{ZrCu}	10.3	9.0	6.0	6.5	4.3	4.1
N_{ZrZr}	5.6	6.1	7.4	8.2	8.6	8.9
N_{Cu}	11.5	11.4	11.0	9.9	10.9	10.4
N_{Zr}	15.9	15.1	13.4	14.6	12.9	13.3
N_{Total}	13.1	12.8	12.2	12.3	12.0	12.1

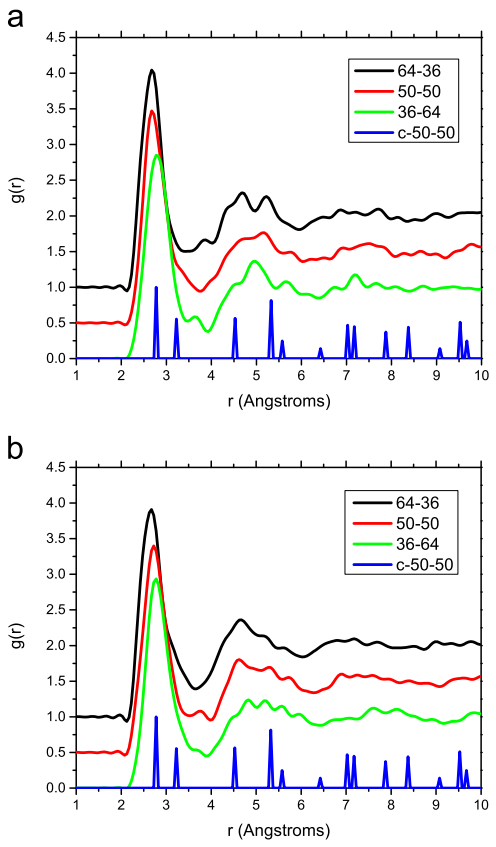

Fig. 2. PDFs of the resulting amorphous structures using (a) DTS and (b) 3DTS. The crystalline positions correspond to the stable B2 crystalline phase of $Cu_{50}Zr_{50}$.

The above mentioned behavior is also observed in the total PDFs in Fig. 4. Once more we see that upon adding zirconium the first peaks move towards larger distances, i.e., towards the crystalline first neighbor distance of pure zirconium. In particular, the DTS $Cu_{36}Zr_{64}$

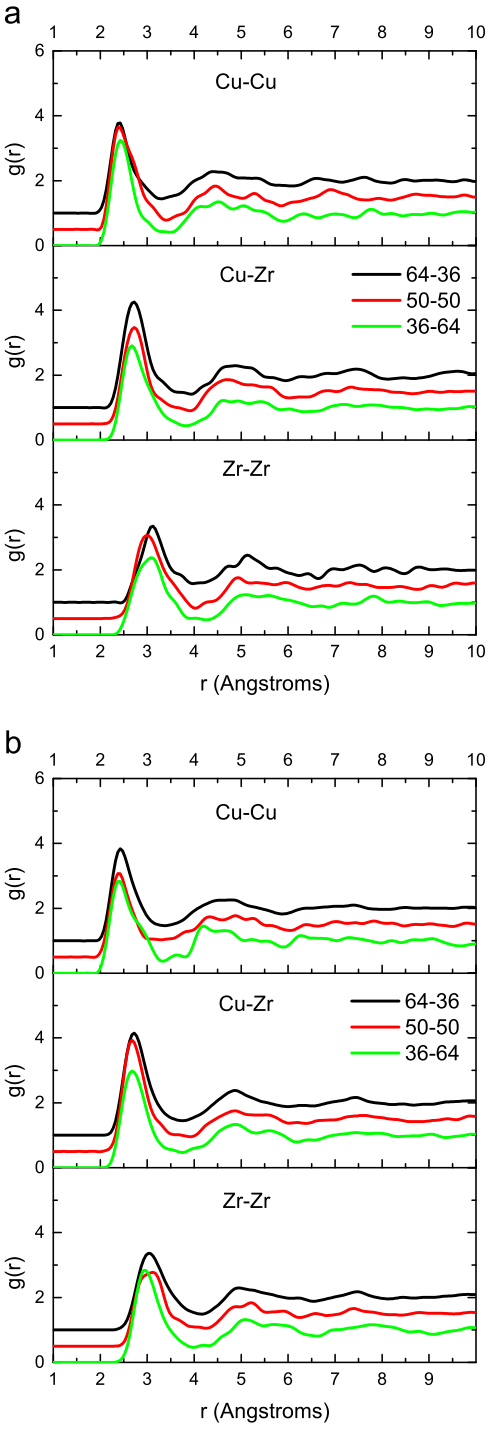

Fig. 3. pPDFs of the resulting liquid structures using (a) DTS and (b) 3DTS.

exhibits a well-defined bimodality in the first coordination peak which of course does not correspond to a liquid-like behavior. This strengthens the fact that DTS is not so adequate to generate liquids using the *undermelt-quench*-based methodology.

We computed the partial coordination numbers for all amorphous and liquid structures using the expression $N_{ij} = \int_0^{r_1} J_{ij}(r)\,dr$, where J_{ij} is the partial radial distribution functions: $J_{ij}(r) = 4\pi r^2 \rho_{ij}$ (pRDFs) the values of r_1 are the positions of the first minima of the pRDFs, ρ_{ij} is the average density of j-type atoms around i-type atoms defined as $\rho_{ij} = \rho_0 c_j g_{ij}(r)$, with ρ_0 the number density, c_j the concentration of j-type atom, and $g_{ij}(r)$ the corresponding pPDF. Total coordinations were obtained by adding the partial

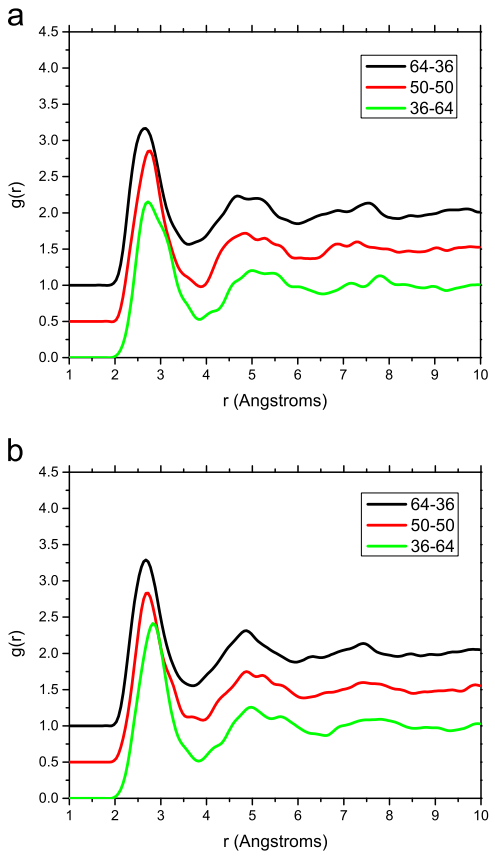

Fig. 4. PDFs of the resulting liquid structures using (a) DTS and (b) 3DTS.

coordination numbers N_{ij}. All coordination values are reported in Table 1.

In the case of the partial N_{ij} and total N we see that both Cu–Cu and Cu–Zr values decrease as Cu is removed from the alloy which is also the case of the total coordination, while Zr–Zr increases as expected. Such tendency is also present in the liquid samples. The fact that the total coordination number decreases and the position of the first peak increases as Zr prevails in the alloy is related to the possible SRO geometries adopted, and of course this has to do with the atomic sizes, i.e., the first neighbor atoms rearrange as Zr atoms are added by moving slightly far from the reference atom due to the zirconium size. This is also verified from Figs. 1 and 3 in Zr–Zr pPDF where first and second neighbor distances are increased upon Zr addition; this tendency is to be expected and was previously discussed in [19], and also seen in [11].

Furthermore, although our partial coordinations vary somewhat with respect to other simulational studies, the discrepancy of the total coordinations with the experimental values is always less than 6% for the amorphous. More interesting are the results for the liquid structures. Surprisingly, although it is well known that total coordination numbers are generally reported by experimentalists, and thus is one of the features that should be compared to validate one's modeling results, in Ref. [11] neither the total PDFs nor the total *N's* for the undercooled and liquid samples were reported, although they could be easily obtained from pPDFs and partial N_{ij}.

When comparing with Jakse and Pasturel we found a slight difference with their partial values. We also can see that the values of N for the total PDFs vary from the ones reported in [19] where they obtained a 13.7 value for the 33.3–66.7 concentration while we obtain a value of 12.0 for both DTS and 3DTS; they obtained 13.6 for their 50–50 sample whereas we have a value of 12.2 for both time steps. We believe that such discrepancies arise from the fact that the experimental value N was calculated by integrating the RDF up to the corresponding first minima of the total PDFs; we used such method for the pPDFs only, which means that the experimental N value may include spurious contributions from second neighbors overestimating the coordination, contrary to our case where we reduced such contributions by adding N_{ij} to obtain the total N.

We have then that DTS has a direct influence on the final structures since some contributions from the initial crystalline configurations still appear in the region between the first and second peaks of the corresponding pPDF and PDFs as mentioned above. On the other hand, a larger time step (3DTS) lets the dynamics of the system evolve better within the *undermelt-quench* framework without atomic overlaps, atomic collisions or without compromising the SCF convergence. Therefore this strengthens the fact, as previously proven [44,45], that 3DTS is the best time step to generate an amorphous structure with the *undermelt-quench* method. Then we consider that 3DTS samples are more representative and these are the ones that we shall compare with experiment.

In Fig. 5 we show a comparison of our amorphous alloys with experimental XRD results of Mattern et al. [7] and Mendelev et al. [15]. We make this total PDF comparison along with first peak positions and coordination number, because other *ab initio*-only simulations either provide the pPDFs or PDFs, and do not properly contrast their results with experiment. We notice that our PDFs and the experimental ones manifest a very good agreement. In the case of our amorphous 64–36 concentration the resemblance is remarkable not only in the first peak but all along the whole 1–10 Å range. In the case of the 50–50 there are slight differences in the first peak right shoulder and in a small bump around 3.75 Å, which might be due to the presence of atoms between the first and second coordination shells upon cooling. As for the 36–64 concentration, our curve is displaced somewhat to shorter distances which means that in the SRO regime some atoms move slightly towards each other pushing other atoms in between first and second neighbor distances, contrary to the 50–50 case, in which is represented as a very small bump around 3.75 Å. We also compare the 64–36 concentration with Wang et al. (Fig. 6a)

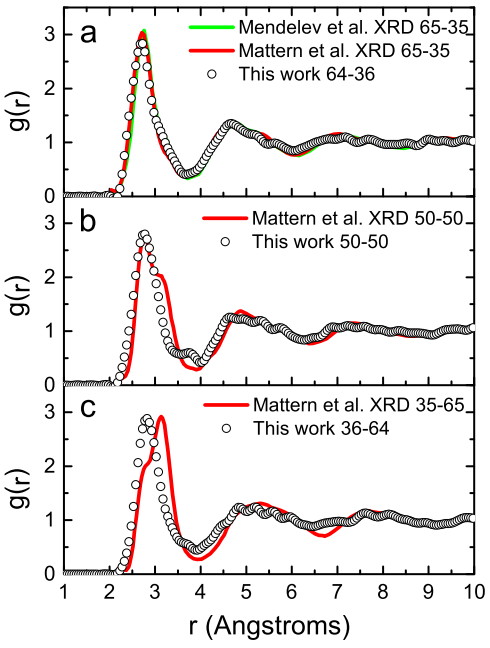

Fig. 5. Total PDF comparison of our 3DTS-generated amorphous samples with experimental XRD.

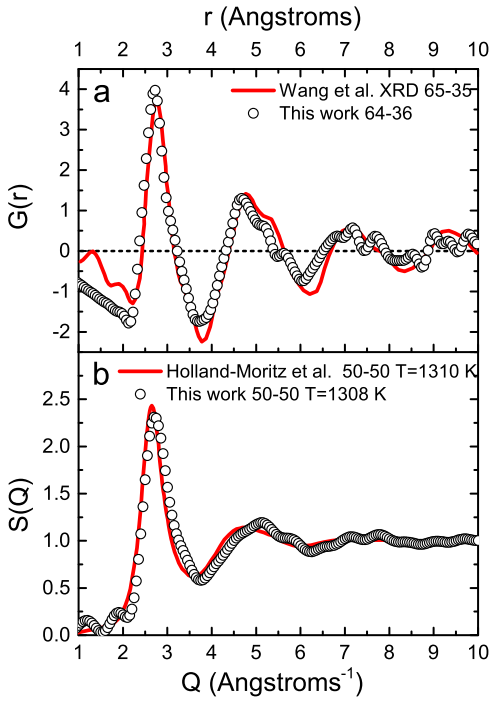

Fig. 6. (a) Total 3DTS-generated amorphous reduced PDF, $G(r)$, comparison with experimental XRD and (b) total structure factor comparison of our liquid 50–50 sample at $T=1308$ K with experimental liquid at $T=1310$ K.

noticing a good agreement of our reduced PDF, $G(r)$, apart from minor discrepancies in the second peak.

Our liquid samples are compared also with experiment. In Fig. 6b we show the total structure factor $S(Q)$ of our 50–50 liquid alloy which exhibits a nice agreement with experiment as well; however some differences arise. The first peak of our study is predicted to be at $Q=2.70$ Å^{-1}, while experimentally it is reported to be at $Q=2.65$ Å^{-1}, which represents an error of 2%.

Since the Bhatia–Thornton [46] S_{NN} partial structure factor provides information about the mean square fluctuations in the particle number, i.e., topological information about atom ordering, in Fig. 7 we show the calculated S_{NN} of our 50–50 and 36–64 liquid alloys and we compare them with experimental liquids reported by Holland-Moritz et al. and Jakse and Pasturel. From the comparison we see that our results are displaced to slightly higher Q values; however, for the 50–50 case we notice a better agreement with experiment than the work reported in [11] for the 46–54 concentration. Differences arise in the case of our 36–64 alloy in the height of the first peak and the first minimum, as well as in the second peak bimodality.

Likewise, we show in Fig. 8a comparison of our liquid pPDFs with the ones obtained by Jakse and Pasturel noticing great similarities apart from slight variations in the heights of the first peaks. Nevertheless, for distances beyond 4 Å a displacement of our curves to shorter distances is exhibited which we believe is due to the temperature difference of 167 K between 1333 K and 1500 K.

The knowledge of the PDFs allows us to compute the bond-angle distributions using the interatomic distance between atoms. These interatomic distances were taken as the first minima in the pPDFs; thus, we obtained all partials (not reported) and total BADs as shown in Fig. 9. They all exhibit peaks near the angles 60°, 63.5°, 108° and 116.5° implying a possible presence of icosahedron-like SRO in both the amorphous and liquid samples to some extent; however, the peaks are sharper for the amorphous structures than for the simulated liquids (Fig. 9). This means that the liquid phase is somewhat more homogeneous than the amorphous one

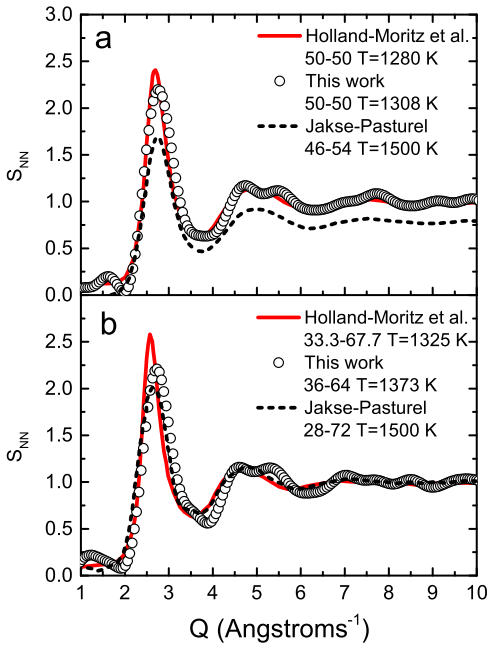

Fig. 7. S_{NN} structure factor comparison of our liquid samples with the corresponding experimental XRD compositions of [19] and with simulations reported in [11].

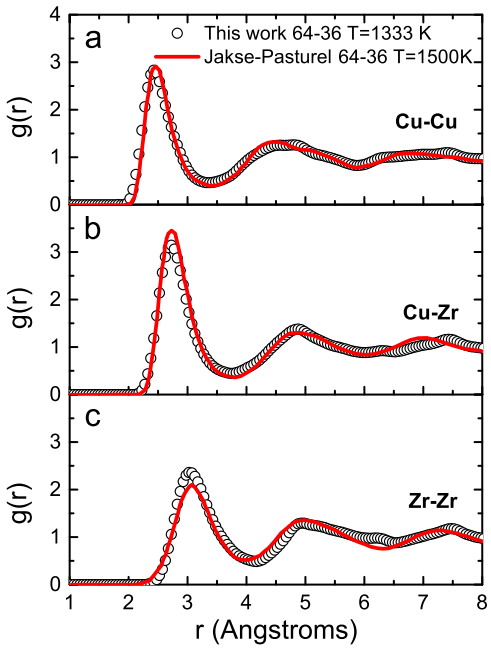

Fig. 8. pPDF comparison of our liquid samples with the theoretical 64–36 liquid reported in Ref. [11].

because the peaks in the BAD become more diffuse; a signal of the presence of other bong-angles which form other possible SRO geometries. However, the characteristic peaks of an icosahedron-like SRO prevail.

In order to go beyond the BAD results, we performed a coordination-number distribution (CND) analysis to track the presence of possible geometries by counting directly the number of neighbors of each atomic species in our structures. We show in Fig. 10 that icosahedron-like geometry (12 neighbors) stands out as the main geometry. As Zr content increases the possible formation of Cu-centered distorted icosahedra decreases in both the amorphous and liquid sample, but does not vanish. It is also

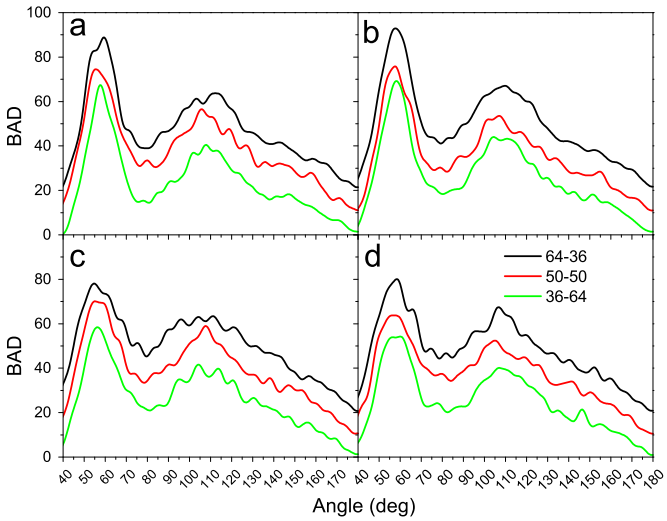

Fig. 9. BAD of the resulting amorphous structures using (a) DTS and (b) 3DTS and of the resulting liquid samples with (c) DTS and (d) 3DTS.

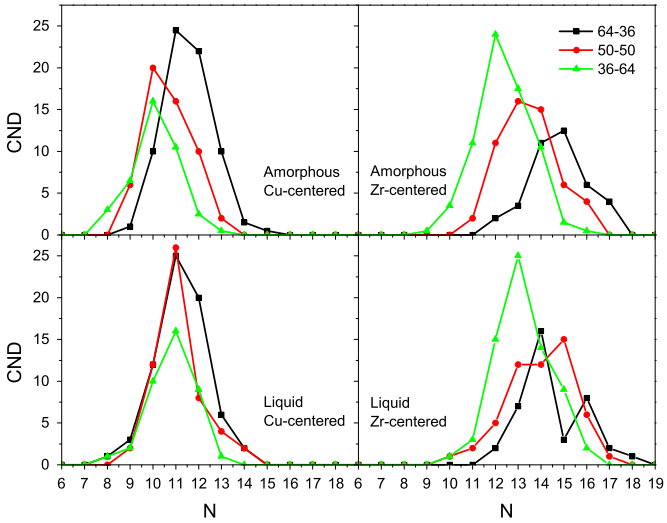

Fig. 10. Coordination number distributions for our amorphous and liquid structures generated with 3DTS.

noteworthy that since angles about 60° prevail in our BADs regardless the composition or phase of the samples, Zr-centered SRO geometries must fit the ones proposed by Frank and Kasper (FK), the so-called FK-*Zn* polyhedra which are geometries associated to the so-called *triangulated coordination shells* [47,48]. Of course these polyhedra do not appear in our structures as ideal but rather distorted due to the disordered nature of our samples and to atomic size differences between copper and zirconium. Thus, Zr-centered polyhedra are mainly *Zn* with $n=13$, 14, 15, 16, 17 and even 18 for liquid 64–36 concentration, exhibiting a decrement in n as zirconium is added; there are also a few Cu-centered Z13 and Z14. Although there are some results which pointed out that such behavior is expected in some BMGs [49], the case of the Cu–Zr 50–50 and 36–64 concentrations reported in our work have not been considered explicitly elsewhere, besides SRO geometries in liquid Cu–Zr alloys as a function of concentration have not been widely discussed.

By weighting the presence of atoms with 12 bonds in the corresponding structures we tracked the percentage of atoms that might exhibit icosahedron-like SRO (Fig. 11). We found that liquid samples tend to have a lower percentage than the amorphous ones agreeing with the experimental report of Holland-Moritz

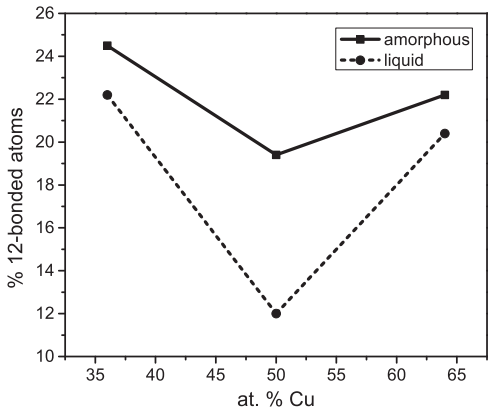

Fig. 11. 12-bonded atoms percentage calculated from the CND for our amorphous and liquid structures.

et al. [19]. Surprisingly, we also found that the number of atoms with 12-bonds is the lowest for both amorphous and liquid 50–50 samples. Recalling the analysis of the total and partial PDFs for our amorphous 50–50 concentration we confirm the phase competition that the system undergoes, where the B2 stable phase is characterized by a bcc configuration whose angles are 70.32°, 109.47° and 180°, whose contributions—although not clearly observed in Fig. 9a and b for amorphous samples—are undoubtedly different from zero.

From the CND analysis we believe that the presence of such complex geometries in our samples is a consequence not only of the packing among nearby atoms, but it is also related to the chemical bonding of atoms depending on how the local atomic environment changes, which in turn is a direct effect of the electronic interactions; i.e., mixing of *s*, *p*, and *d* orbitals of every atomic species should play a role in bonding that leads to different SRO configurations. For this reason a more extensive study of the electronic properties of amorphous and liquid Cu–Zr alloys [34] must be carried out that aims at providing a better understanding of the interactions and contributions of every component to bonding.

4. Conclusions

By applying two variants of the *undermelt-quench* method, we generated amorphous and liquid Cu–Zr alloys that show a good structural agreement with other simulations and with available experiments. We found that the amorphous 50–50 concentration undergoes a phase competition with the stable B2 crystalline structure upon cooling; however, this is more obvious when using the default time step because due to the slower dynamics, the system tends to reach the crystalline stable $Cu_{50}Zr_{50}$ phase rather than the disordered phase. Coordination numbers show a tendency to decreasing icosahedron-like SRO upon Zr addition in amorphous structures, and although liquid samples show a lower icosahedron-like SRO, a similar tendency is observed. We found several signals that lead us to conclude that icosahedron-like SRO plays a dominant role in either amorphous or liquid structures; moreover, a range of possible geometries appear which include FK *Zn* polyhedra due to the prevailing peaks in the BADs around 60°, related to the so-called triangulated coordination shells, regardless of the atomic type located at the center of the polyhedra. Our results agree with other simulational reports, but most importantly with the amorphous and liquid structures generated experimentally; this in turn would allow us to calculate other interesting properties that have long been disregarded in the literature: the electronic and vibrational ones, that would aid to

understand the diverse phenomena that take place in these exceptional materials.

Acknowledgments

J. Galván-Colín acknowledges CONACyT for supporting his Ph.D. studies. A.A.V., R.M.V. and A.V. thank DGAPA-UNAM for continued financial support to carry out research projects IN101798, IN100500, IN119105, IN119908, IN112211 and IN110914. M.T. Vázquez and O. Jiménez provided the information requested. Parts of the simulations were performed in DGTIC-UNAM Center.

References

[1] W. Klement, R.H. Willens, P. Duwez, Nature 187 (1960) 869–870.
[2] M. Miller, P. Liaw, in: M. Miller, P. Liaw (Eds.), Bulk Metallic Glasses—An Overview, Springer Science and Business Media, NY, USA, 2008, pp. xi–xii.
[3] D. Xu, B. Lohwongwatana, G. Duan, W.L. Johnson, C. Garland, Acta Mater. 52 (2004) 2621–2624.
[4] D. Wang, Y. Li, B.B. Sun, M.L. Sui, K. Lu, E. Ma, Appl. Phys. Lett. 84 (2004) 4029–4031.
[5] W.H. Wang, J.J. Lewandowski, A.L. Greer, J. Mater. Res. 20 (2005) 2307–2313.
[6] G. Duan, D. Xu, Q. Zhang, G. Zhang, T. Cagin, W.L. Johnson, W.A. Goddard, Phys. Rev. B 71 (2005) 2242081–2242089.
[7] N. Mattern, P. Jóvari, I. Kaban, S. Gruner, A. Elsner, V. Kokotin, H. Franz, B. Beuneu, J. Eckert, J. Alloys Compd. 485 (2009) 163–169.
[8] X.D. Wang, S. Yin, P. Cao, J.Z. Jiang, H. Franz, Z.H. Jin, Appl. Phys. Lett. 92 (2008) 0119021–0119023.
[9] Y.A. Babanov, V.R. Schvetsov, A.F. Siderenko, Physica B 208–209 (1995) 375–376.
[10] M. Bionducci, G. Licheri, G. Navarra, B. Bouchet-Fabre, Z. Naturforsch. A 51 (1996) 71–82.
[11] N. Jakse, A. Pasturel, Phys. Rev. B 78 (2008) 2142041–2142049.
[12] A.E. Lagogianni, G. Almyras, C.E. Lekka, D.G. Papageorgiou, G.A. Evangelakis, J. Alloys Compd. 483 (2009) 658–661.
[13] G.A. Almyras, D.G. Papageorgiou, C.E. Lekka, N. Mattern, J. Eckert, G. Evangelakis, Intermetallics 19 (2011) 657–661.
[14] J. Antonowicz, A. Pietnoczka, T. Drobiazg, G.A. Almyras, D.G. Papageorgiou, G. Evangelakis, Philos. Mag. 92 (2012) 1865–1875.
[15] M.I. Mendelev, M.J. Kramer, R.T. Ott, D.J. Sordelet, M.F. Besser, A. Kreyssig, A. I. Goldman, V. Wessels, K.K. Sahu, K.F. Kelton, R.W. Hyers, S. Canepari, J. R. Rogers, Philos. Mag. 90 (2010) 3795–3815.
[16] M. Li, C.Z. Wang, S.G. Hao, M.J. Kramer, K.M. Ho, Phys. Rev. B 80 (2009) 1842011–1842017.
[17] C. Valencia-Balvín, C. Loyola, J. Osorio-Guillén, G. Gutiérrez, Physica B 405 (2010) 4970–4977.
[18] Y.L. Sun, J. Shen, A.A. Valladares, J. Appl. Phys. 106 (2009) 0735201–0735208.
[19] D. Holland-Moritz, F. Yang, T. Kordel, S. Klein, F. Kargl, J. Gegner, T. Hansen, J. Bednarcik, I. Kaban, O. Shuleshova, Europhys. Lett. 100 (2012) 56002 (1-6).
[20] S.G. Hao, C.Z. Wang, M.J. Kramer, K.M. Ho, J. Appl. Phys. 107 (2010) 0535111–0535116.
[21] A.A. Valladares, F. Alvarez, Z. Liu, J. Stitch, J. Harris, Eur. Phys. J. B 22 (2001) 443–453.
[22] A.A. Valladares, A New Approach to the Ab Initio Generation of Amorphous Semiconducting Structures, Electronic and Vibrational Studies, Nova Publisher Science, New York (2008), p. 61–123.
[23] E.Y. Pe na, M. Mejía, J.A. Reyes, R.M. Valladares, F. Álvarez, A.A. Valladares, J. Non-Cryst. Solids 338–340 (2004) 258–261.
[24] C. Romero, Z. Mata, M. Lozano, H. Barrón, R.M. Valladares, F. Álvarez, A. A. Valladares, J. Non-Cryst. Solids 338–340 (2004) 513–516.
[25] A. Valladares, R.M. Valladares, F. Álvarez-Ramírez, A.A. Valladares, J. Non-Cryst. Solids 352 (2006) 1032–1036.
[26] L.M. Mejía-Mendoza, R.M. Valladares, A.A. Valladares, Mol. Simul. 34 (2008) 989–995.
[27] J.A. Reyes-Retana, A.A. Valladares, Comput. Mater. Sci. 47 (2010) 934–939.
[28] A.A. Valladares, J. Non-Cryst. Solids 353 (2007) 3540–3544.
[29] J.A. Díaz-Celaya, A.A. Valladares, R.M. Valladares, Intermetallics 18 (2010) 1818–1820.
[30] L. Yang, J.H. Xia, Q. Wang, C. Dong, L.Y. Chen, X. Ou, J.F. Liu, J.Z. Jiang, K. Klementiev, K. Saksl, H. Franz, J.R. Schneider, L. Gerward, Appl. Phys. Lett. 88 (2006) 2419131–2419133.
[31] J. Hafner, J. Phys. F: Met. Phys. 12 (1982) L205–L209.
[32] J. Hafner, J. Phys. Colloq. C C9 (46) (1985) 69–78.
[33] A. DiCicco, A. Trapananti, S. Faggioni, A. Filipponi, Phys. Rev. Lett. 91 (2003) 1355051–1355054.
[34] J. Galván-Colín, A.A. Valladares, R.M. Valladares, in preparation.
[35] B. Delley, J. Chem. Phys. 92 (1990) 508–517.
[36] B. Delley, J. Chem. Phys. 113 (2000) 7756–7764.
[37] B. Delley, Phys. Rev. B 66 (2002) 1551251–1551259.
[38] J.P. Perdew, Y. Wang, Phys. Rev. B 45 (1992) 13244–13249.
[39] P.R. Subramanian, D.J. Chakrabarti, D.E. Laughlin, Phase Diagrams of Binary Copper Alloys, Materials Information Society, Ohio, 1994.
[40] T. Aiyama, T. Fukunaga, K. Niihara, T. Hirai, K. Suzuki, J. Non-Cryst. Solids 33 (1979) 131–139.
[41] M. Misawa, T. Fukunaga, K. Niihira, T. Hirai, K. Suzuki, J. Non-Cryst. Solids 34 (1979) 313–321.
[42] T. Fukunaga, T. Goto, M. Misawa, T. Hirai, K. Suzuki, J. Non-Cryst. Solids 95–96 (1987) 1119–1125.
[43] A.J.C. Wilson, International Tables for Crystallography C, 3rd ed., Dordrecht, Kluwer Academic Publishers, 2004.
[44] A.A. Valladares, J.A. Díaz-Celaya, J. Galván-Colín, L.M. Mejía-Mendoza, J. A. Reyes-Retana, R.M. Valladares, A. Valladares, F. Alvarez-Ramirez, D. Qu, J. Shen, Materials 4 (2011) 716–781.
[45] J. Galván-Colín, Método computacional *ab initio* para amorfizar una aleación Cu-Zr ($Cu_{64}Zr_{36}$), M.Sc. thesis, Universidad Nacional Autónoma de México, México, 2011.
[46] A.B. Bhatia, D.E. Thornton, Phys. Rev. B 2 (1970) 3004–3012.
[47] F.C. Frank, J.S. Kasper, Acta Crystallogr. 11 (1958) 184–190.
[48] F.C. Frank, J.S. Kasper, Acta Crystallogr. 12 (1959) 483–499.
[49] H.W. Sheng, W.K. Luo, F.M. Alamgir, J.M. Bai, E. Ma, Nature 439 (2006) 419–425.